

---

# **DEVELOPMENT OF A COMPRESSIVE SENSING BASED BEAMFORMING DEMONSTRATOR FOR 2D ULTRASOUND PLANE WAVE IMAGING**

---

Semester project submitted to

Signal Processing Laboratory (LTS5)  
École Polytechnique Fédérale de Lausanne

**Author:** Eric Francis Bezzam

**Supervisor:** Prof. Jean-Phillipe Thiran

June 13, 2016

# Contents

<b>List of Figures</b>	<b>2</b>
<b>1 Introduction</b>	<b>4</b>
<b>2 Theoretical Background</b>	<b>6</b>
2.1 Ultrasound Imaging . . . . .	6
2.1.1 Conventional Imaging Method . . . . .	7
2.1.2 Plane Wave Imaging . . . . .	7
2.2 Compressive Sensing . . . . .	9
2.2.1 Compressive Sensing Basics . . . . .	9
2.2.2 Problem Formulation for Ultrasound Imaging . . . . .	10
2.2.3 Requirements for Ultrasound Imaging . . . . .	11
2.3 Full Process for Conventional and Compressive Sensing Based Plane Wave Imaging . . . .	11
<b>3 Demonstrator</b>	<b>12</b>
3.1 Complete Setup . . . . .	12
3.2 Background on the ULA-OP System . . . . .	13
3.2.1 Hardware . . . . .	13
3.2.2 Software . . . . .	13
3.3 Custom Software for the Demonstrator . . . . .	14
3.3.1 Graphical User Interface . . . . .	15
3.3.2 Full Capabilities in MATLAB . . . . .	16
3.3.3 Main ULA-OP Configuration Issues and Solutions . . . . .	16
<b>4 Results and Analysis</b>	<b>19</b>
4.1 Uniform vs. Random Sampling . . . . .	20
4.2 Coherent Plane Wave Compounding . . . . .	20
4.3 Varying Number of Transducers . . . . .	21
4.4 Choosing a Proper Representation Basis . . . . .	21
4.5 Imaging Large Ranges . . . . .	22
<b>5 Conclusion</b>	<b>24</b>
<b>Bibliography</b>	<b>25</b>

# List of Figures

2.1	Comparing methods for B-mode imaging. Left-most image corresponds to the conventional method of insonifying one scan line at a time. The following three images each demonstrate plane wave imaging with a different amount of insonifications, as indicated at the top of each image. Taken from [7]. . . . .	6
2.2	Steered plane wave time-of-flight visualization. Adapted from [9]. . . . .	7
2.3	Frequency spectrum of an RF signal acquired by a 2.5 MHz probe. Taken from [10]. . . . .	8
2.4	A dirac in the image domain is spread out in the frequency domain. Random sampling in the frequency domain should be able to reconstruct the dirac under the CS framework. Taken from [11]. . . . .	10
3.1	Physical setup for the 2D CS-based PW imaging demonstrator. . . . .	12
3.2	GUI for the developed software for 2D CS-based PW imaging. . . . .	15
4.1	CIRS Model 054GS General Purpose US Phantom [21]. . . . .	19
4.2	B-mode images of the region surrounded in red and labeled “1” in Figure 4.1. Random spacing, (a) and (c), is compared with uniform spacing, (b) and (d), as a sensing scheme. Figures (a) and (b) use 12.5% of the elements while Figures (c) and (d) use 25% of the elements. A single PW with $0^\circ$ incident angle is transmitted and the CS-based method with $\beta_L = 0.018$ is used for image reconstruction. . . . .	20
4.3	B-mode images of the region surrounded in red and labeled “1” in Figure 4.1. A different number of PWs is transmitted for each image to show the effect of compounding. The CS-based approach with $\beta_L = 0.018$ is applied for image reconstruction. Only 5% of the probe elements (uniformly spaced) are used. . . . .	20
4.4	B-mode images of the region surrounded in red and labeled “1” in Figure 4.1. The number of uniformly-spaced active elements is varied for each image: 10%, 12.5%, 25%, and 50% of the 128 elements. A single PW with $0^\circ$ incident angle is transmitted and the CS-based PW beamforming method with $\beta_L = 0.018$ is used for image reconstruction. . . . .	21
4.5	B-mode images of the region surrounded in red and labeled “1” in Figure 4.1. The number of uniformly-spaced active elements is varied for each image: 10%, 12.5%, 25%, and 50% of the 128 elements. A single PW with $0^\circ$ incident angle is transmitted and the conventional PW beamforming method is used for image reconstruction. . . . .	21
4.6	B-mode images of the region surrounded in blue and labeled “2” in Figure 4.1. Five PWs, linearly spaced from $-2^\circ$ to $2^\circ$ , were transmitted using 12.5% elements of the probe, uniformly spaced. CS-based PW beamforming with compounding is used in (a)-(c) for image reconstruction: (a) uses the <i>Orthogonal Wavelet</i> basis with $\beta_L = 0.04$ , (b) uses the <i>Dirac</i> basis with $\beta_L = 0.05$ , and (c) uses the <i>Dirac</i> basis with $\beta_L = 0.05$ . The last image (d) uses conventional PW beamforming with compounding. . . . .	22

# LIST OF FIGURES

4.7	B-mode images of the regions surrounded in blue and green and labeled “2” and “3” in Figure 4.1. Five PWs, linearly spaced from $-2^\circ$ to $2^\circ$ , were transmitted using 12.5% elements of the probe, uniformly spaced. CS-based PW beamforming with compounding is used in (a)-(b) for image reconstruction: (a) uses the <i>Dirac</i> basis with $\beta_L = 0.05$ and (b) uses the <i>Dirac</i> basis with $\beta_L = 0.5$ . The last image (c) uses conventional PW beamforming with compounding. . . . .	23
-----	--	----

# 1 Introduction

Ultrasound (US), “a type of sound we cannot hear” [1], can be classified as frequencies over 20 kHz, the human threshold for hearing. During the past several decades, medical US has established itself as a widely-used tool in the area of diagnostic imaging. Its main advantages over other common imaging modalities, such as X-rays, computed tomography (CT) scans, and magnetic resonance imaging (MRI), include low-cost, computational speed, and portability [1]. Moreover, US is non-invasive and does not emit ionizing radiation, which could produce harmful biological side effects that accumulate over time. There are, however, some key limitations to the use of US as an imaging technique. A high level of skill and experience is needed to both acquire and interpret US images. This is primarily due to the fact that the quality of the obtained images, measured in terms of *resolution* and *contrast*, is relatively poor, especially in comparison with the previously mentioned imaging techniques. Moreover, the quality worsens when attempting to image at deeper depths. This occurs because of the attenuation of US waves during propagation through human tissue. There are several sources of losses: reflection, refraction,  $1/r$  or spreading loss, scattering, and absorption [1]. As these numerous sources of attenuation can lead to low-quality images, an expert is needed to correctly understand what has been captured and displayed in a typical 2D US image. Furthermore, a correct handling of the probe is required in order to properly acquire the desired anatomical structures as a very constraint protocol and path may be necessary. Through the use of 3D US imaging, volumetric information can be obtained, which can help relax the constraints on the handling of the probe and alleviate the difficulty of correctly interpreting the measurements as a 3D visualization is possible.

As US has already proven to be portable and cheap, the integration of 3D imaging in commercial products could broaden its possible uses. The UltrasoundToGo project intends to do just this by developing “a high performance, low-power signal processing platform for US imaging applications, targeting future 3D portable US systems” [2]. One objective of this project is to facilitate the acquisition and analysis of US images so that general practitioners and unskilled operators could make use of it and consult a specialist if need be. However, 3D imaging is faced with a significant limitation: data storage and the associated computation required by the increase in data. According to [3], a 3D image requires about  $2.5 \times 10^{12}$  delay values/s for reconstruction at 15 frames/s, and this is well beyond the capabilities of any available off-chip memory interface. The LTS5 laboratory at EPFL has proposed and is currently developing a solution to this problem by reducing the amount of data required to reconstruct a meaningful image. This is accomplished through compressive sensing (CS) techniques.

The goal of this semester project was to incorporate these techniques with a real US system as to provide a proof-of-concept of CS reconstruction for 2D US plane wave (PW) imaging. As UltrasoundToGo is funded by the Nano-Tera Initiative, the results of this project were also demonstrated at the 2016 Nano-Tera Annual Plenary Meeting, which took place from April 25-26 [4].

This report has the following structure: Chapter 2 provides a brief summary of the relevant theory in US imaging and CS; Chapter 3 presents the ULA-OP system for US imaging [5] and what was developed during this project in order to create a demonstrator of 2D CS-based PW imaging; Chapter 4 provides

several results from the developed demonstrator and discusses a few key observations and limitations that can be attained from them; and Chapter 5 summarizes the main accomplishments and findings of the work from this semester project and discusses future work.

## 2 Theoretical Background

This section provides a general overview of the relevant theory in US and CS. A more detailed description of these topics can be found in the referenced literature.

### 2.1 Ultrasound Imaging

As previously mentioned, US waves are frequencies that we cannot hear; they are above what the human ear can perceive. For the use of medical imaging, the typical range of used frequencies is from 1 to 15 MHz [1]. The reason why US can provide a rather accurate representation of tissue geometry is due to the fact that the speed of sound can be approximated as  $c = 1540 \text{ m s}^{-1}$  for most soft tissues [1], *i.e.* the speed of sound does not vary significantly when it goes through different soft tissue media in the human body. Moreover, after using an array of transducers, *i.e.* a *probe*, to emit US waves, we can coherently sum the reflected waves received by the same probe to image inside the human body. This summation of received waveforms is known as *beamforming* and can amplify the signal-to-noise ratio in a desired direction [6].

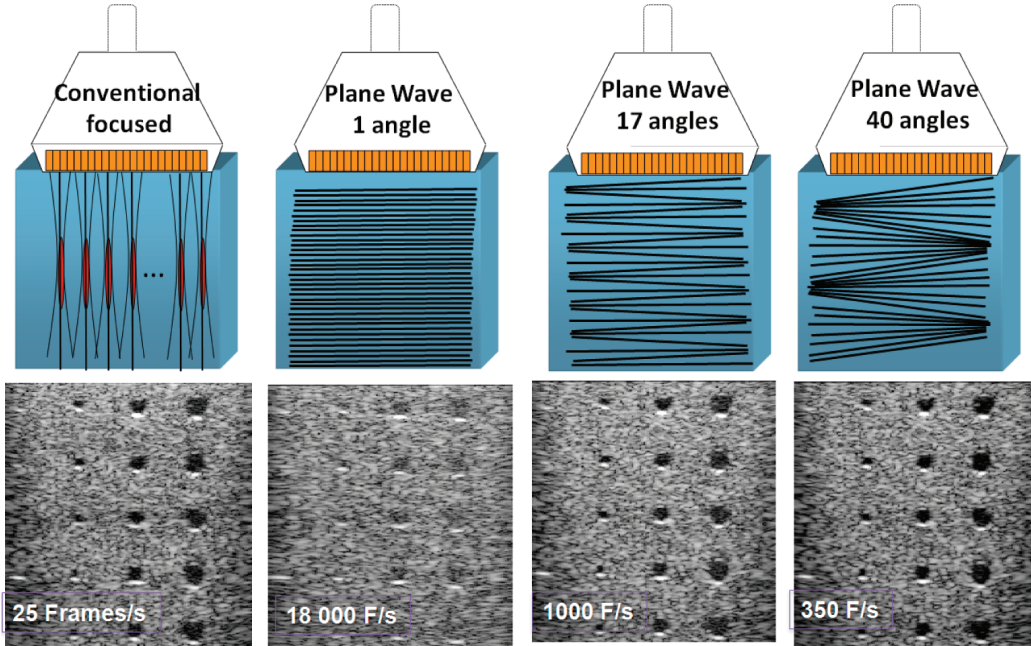


**Figure 2.1** Comparing methods for B-mode imaging. Left-most image corresponds to the conventional method of insonifying one scan line at a time. The following three images each demonstrate plane wave imaging with a different amount of insonifications, as indicated at the top of each image. Taken from [7].

### 2.1.1 Conventional Imaging Method

The most common diagnostic image produced by US waves is the *B-mode* image, short for Brightness-mode, as the brightness is proportional to the echo amplitude [1]. A conventional B-mode image is created by imaging one scan (vertical) line at a time in order to create a 2D image. This process is known as *delay-and-sum* (DAS) beamforming. Each line requires an *insonification*, *i.e.* a transmission of US waves by the probe, focused on that particular lateral section. The conventional process for creating a B-mode image can be seen in the left-most image of Figure 2.1. The frame rate of this approach is upper bounded by:

$$FR_{max} = \frac{c}{2NZ}, \quad (2.1)$$

where  $N$  is the number of lines and  $Z$  is the image depth in meters. The frame rate of DAS beamforming can be severely hampered by the desired image depth and the desired resolution, which determines the number of lines and potential focal points along each line.

### 2.1.2 Plane Wave Imaging

One alternative method to B-mode imaging that has recently garnered a lot of attention is *plane wave* (PW) imaging. With this method, a single insonification can be used to image the whole area of interest, thus allowing for ultrafast frame rates [8]. However, one PW insonification is generally not sufficient as the resulting image has low contrast. The image second from the left in Figure 2.1 shows the result of one PW insonification. The contrast for this one PW insonification is clearly less than the contrast for the conventional B-mode imaging method (left-most image of Figure 2.1).

Through the use of coherent PW compounding, multiple insonifications can be used to significantly improve the contrast of the image while keeping the number of insonifications low enough so that high frame rates are still achieved [9]. The two images on the right of Figure 2.1 show that by increasing the number of PW insonifications, the contrast of the image can be significantly improved while still achieving much higher frame rates than the conventional B-mode imaging method. For this reason, coherent PW imaging for B-mode imaging was implemented and investigated in this project.

#### Plane Wave Image Reconstruction for a Single Angle

As previously mentioned, PW imaging can use a single insonification to image the whole region of interest. However, in order to properly beamform and measure the intensity at a certain point, the time-of-flight needs to be applied as a delay to each of the signals measured by the  $M$  transducers, *i.e.* *channels*, so that the signal values can be summed coherently. Figure 2.2 provides a visualization of the distance traveled by a steered plane wave to the point  $(x_i, z_i)$  and ultimately reflected to a transducer at  $(x_m, 0)$ <sup>1</sup>.

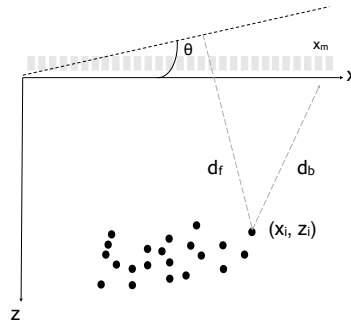


**Figure 2.2** Steered plane wave time-of-flight visualization. Adapted from [9].

<sup>1</sup>When referring to the position of a transducer, the  $z$  value is dropped as it is always 0.



The *forward* distance to point  $(x_i, z_i)$  is given by:

$$d_f = z_i \cos \theta + x_i \sin \theta, \quad (2.2)$$

where  $\theta$  is the angle of the emitted plane wave with respect to one end of the transducer array. The *backward* distance to reach a transducer at  $x_m$  is given by:

$$d_b = \sqrt{z_i^2 + (x_i - x_m)^2}. \quad (2.3)$$

Therefore, the total time-of-flight can be computed by dividing the total distance by the speed of sound in the medium  $c$ :

$$\tau_{x_i, z_i, x_m} = \frac{d_f + d_b}{c} = \frac{z_i \cos \theta + x_i \sin \theta + \sqrt{z_i^2 + (x_i - x_m)^2}}{c}. \quad (2.4)$$

In order to obtain the value at the point  $(x_i, z_i)$ , the  $M$  signal values at  $\tau_{x_i, z_i, x_m}$  for the according channel at  $x_m$  are averaged in order to produce the corresponding intensity:

$$F_\theta(x_i, z_i) = \frac{1}{M} \sum_{m=0}^{M-1} s_m(t - \tau_{x_i, z_i, x_m}), \quad (2.5)$$

where  $F_\theta$  is the resulting beamformed image from a PW steered by angle  $\theta$  in degrees and  $s_m$  is the signal measured by the  $m^{th}$  channel at  $x_m$ .

### Coherent Plane Wave Compounding

One PW insonification is generally not enough to achieve a desirable contrast. Therefore, it is usually necessary to apply coherent PW compounding [9]. If we have  $K$  insonifications at different  $\theta_k$  angles resulting in  $F_{\theta_k}$  corresponding images, the value of the final image  $\bar{F}$  at the point  $(x_i, z_i)$  is given by:

$$\bar{F}(x_i, y_i) = \frac{1}{K} \sum_{k=1}^K F_{\theta_k}(x_i, z_i). \quad (2.6)$$

The positive effects of compounding in improving contrast can be seen from Figure 2.1 and from results obtained by our demonstrator in Section 4.2.

### Post-Processing

After compounding, a few crucial post-processing steps need to be performed to  $\bar{F}$  in order to produce the B-mode image. The beamformed signal  $\bar{F}$  is typically known in the US community as a Radio Frequency (RF) signal. It is a band-pass signal whose bandwidth  $B$  is typically centered around the frequency of the probe as shown in Figure 2.3. Therefore, sampling at a high frequency  $f_s$  leads to more data than what is necessary to describe the acquired signal. The common approach for reducing

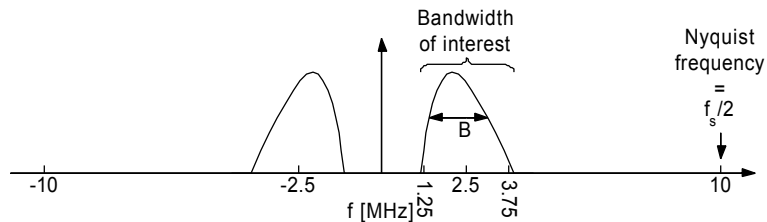


**Figure 2.3** Frequency spectrum of an RF signal acquired by a 2.5 MHz probe. Taken from [10].

the amount of data without losing essential information is by applying a complex base-band modulation technique with bandwidth reduction known as IQ-demodulation [10]. It usually consists of three steps:

1. Down-mixing - shifting the positive half of the spectrum so that it is centered at 0 Hz, *i.e.* baseband;
2. Low-pass filtering - remove the negative half of the spectrum and noise outside the desired bandwidth;
3. Decimation - obtain the necessary amount of sample in order to satisfy the Nyquist criterion.

We will denote the image after post-processing as  $I$ .

### Visualization

Before displaying the B-mode image,  $I$  needs to be normalized to obtain  $I_n$  and then log-compressed as follows:

$$Bmode_{dB} = 20 \log_{10} I_n. \quad (2.7)$$

## 2.2 Compressive Sensing

In recent years, CS has gained a lot popularity in the field of diagnostic imaging. It is already well-established in current commercial MRI technology [11] and has garnered interest in CT scans in order to reduce patient exposure to ionizing radiation [12]. In the realm of US imaging, CS has been investigated due to its potential in yielding higher frame rates by reducing data storage and transfer [13].

Before the introduction of CS, the widely-accepted approach towards acquiring data has been Nyquist's theorem of sampling at least twice the highest frequency component. However, this approach does not assume any prior on the structure of the signal that one is trying to acquire. Moreover, it tends to be the case in medical imaging that we can expect certain structures in the final image. For example, in US imaging, common structures include anechoic and hyperechoic objects, strong point reflectors, and speckle. Different priors in the form of a basis or a pre-dictionary can be used to extract such structures from under-sampled data through the CS framework.

### 2.2.1 Compressive Sensing Basics

#### Sparsity and Incoherence

CS relies on two principles: *sparsity* in the signal of interest and *incoherence* in the sensing modality [14]. Sparsity refers to the idea that the number of degrees of freedom is much smaller than the size of the discrete measurement. Moreover, a signal  $\mathbf{x}$  is  $K$ -sparse if it can be expressed in terms of some basis or pre-defined dictionary  $\Psi$  as:

$$\mathbf{x} = \Psi \mathbf{s}, \quad (2.8)$$

where  $\mathbf{s} \in \mathbb{R}^N$  is a vector of weights and its number of non-zero components  $K$  is much smaller than  $N$ , *i.e.*  $K \ll N$  [15]. The basis or dictionary  $\Psi$  is referred to as the *representation* matrix.

The second core principle of CS, namely incoherence, requires that the objects having a sparse representation in  $\Psi$  must be spread out in the domain in which they are acquired [14]. If the signal which is sparse in  $\Psi$  has a dense representation in the *sensing* domain  $\Phi$ , an under-sampling of the data in the sensing domain should be sufficient to reconstruct the original signal in the representation domain. This phenomenon of incoherence can be observed from Figure 2.4. Even though the under-sampled data in the FFT domain produces a noisy version of the original signal when we take it back to the image domain through the IFFT (yielding a dirac with low amplitude noise), using the constraint of sparsity we can recover the original signal (a single dirac).

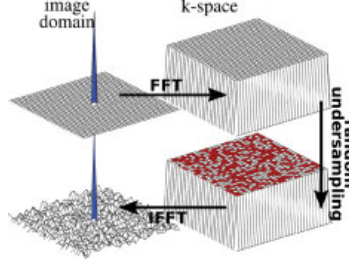


**Figure 2.4** A dirac in the image domain is spread out in the frequency domain. Random sampling in the frequency domain should be able to reconstruct the dirac under the CS framework. Taken from [11].

The coherence between the sensing basis  $\Phi$  and the representation basis  $\Psi$  can be written as:

$$\mu(\Phi, \Psi) = \sqrt{N} \max_{1 \leq k, j \leq N} |\langle \phi_k, \psi_j \rangle|, \quad (2.9)$$

where  $N$  is the number of basis vectors in  $\Psi$ . Incoherence implies a low value for  $\mu$  [14].

### Minimum $\ell_1$ Norm Reconstruction

The  $\ell_2$  norm is a typical choice for minimizing error, such as in linear regression. However, the  $\ell_2$  norm measures signal energy and not signal sparsity. The  $\ell_0$  norm, on the other hand, counts the number of non-zero entries in a vector, which is ideal for measuring signal sparsity. Unfortunately, minimizing an  $\ell_0$  norm is combinatorial, requiring an exhaustive search for the  $K$  non-zero entries in a length  $N$  vector [15].

Fortunately, minimization with the  $\ell_1$  norm can exactly recover  $K$ -sparse signals and closely approximate compressible<sup>2</sup> signals with high probability [15]. The choice of the  $\ell_1$  norm allows for convex relaxation of the  $\ell_0$  optimization problem so that already-known algorithms for solving  $\ell_1$  optimization problems can be used, such as Orthogonal Matching Pursuit or ADMM (Alternative Direction Method of Multipliers) [16].

### 2.2.2 Problem Formulation for Ultrasound Imaging

In the case of US imaging, it is our observed beamformed signal  $\mathbf{F} \in \mathbb{R}^{N \times M}$  that we assume to have a sparse representation rather than the original signal  $\mathbf{X} \in \mathbb{R}^{N \times M}$ , *i.e.* the reflected echoes. The values  $N$  and  $M$  refer to the number of samples, which is related to the depth and to the number of channels respectively.

Let us assume that  $\mathbf{f} \in \mathbb{R}^P$ , a vectorized version of  $\mathbf{F}$  with a length of  $P = N \times M$ , has a sparse representation in  $\Psi$ . In order to induce this sparsity, we wish to minimize the following  $\ell_1$  norm:

$$\min_{\hat{\mathbf{f}} \in \mathbb{R}^P} \|\Psi \hat{\mathbf{f}}\|_1 \text{ subject to } \|\mathbf{x} - \Phi \hat{\mathbf{f}}\|_2 \leq \beta, \quad (2.10)$$

where  $\mathbf{x} \in \mathbb{R}^P$  is a vectorized version of  $\mathbf{X}$ ,  $\Phi$  is the sensing basis, and the  $\ell_2$  constraint promotes signal integrity according to a tolerance level  $\beta$ . The sensing operation  $\Phi$  is actually related to the inverse of the beamforming operation, which is used to obtain the beamformed data  $\mathbf{F}$  from the raw data  $\mathbf{X}$ . In this report, raw data refers to the signals acquired by each channel *before* beamforming. This inverse problem tends to be ill-posed but the sparse prior on  $\mathbf{f}$  regularizes the solution.

An  $\ell_1$  minimization, however, is not as straightforward to solve as an  $\ell_2$  minimization as there is no

<sup>2</sup>A signal  $\mathbf{x}$  is *compressible* if the representation in (2.8) has just a few large coefficients and many small coefficients [15].

closed-form solution such as the Wiener Filter for  $\ell_2$ . Therefore, we use the ADMM approach to solve the  $\ell_1$  minimization iteratively. A detailed description of this method can be found in [16]. It is worth noting, however, that there are two important parameters for this method: the number of iterations and a threshold level  $\beta_L$  which sets to zero anything in the range  $[-\beta_L, \beta_L]$  at each iteration step. This is known as *soft-thresholding*. A higher  $\beta_L$  induces more sparsity while a low  $\beta_L$  is less selective.

### 2.2.3 Requirements for Ultrasound Imaging

There are two main requirements for the use of CS in US reconstruction:

1. Finding an appropriate sensing strategy to acquire the echoes with a reduced number of channels;
2. Finding the proper representation basis to model the acquired signals.

For the first requirement, two sensing strategies were investigated and implemented in the final demonstrator: uniform and random sampling with varying amounts of active, *i.e.* used, channels. A uniform spacing of channels keeps the same distance between sensors. Random spacing spans the whole array by using the outermost channels; however, the rest of the sensors are selected randomly.

For the second requirement, several bases are considered: Dirac (simple case where  $\Psi$  is equal to identity), Orthogonal Wavelet [17], Undecimated Wavelet [18], and SARA [19].

Therefore, the important CS parameters for the demonstrators are:

1. The spacing and number of active elements of the probe;
2. The representation basis -  $\Psi$ ;
3. The signal integrity threshold -  $\beta$  (see Equation 2.10);
4. The ADMM parameters -  $\beta_L$  soft-threshold and number of iterations.

## 2.3 Full Process for Conventional and Compressive Sensing Based Plane Wave Imaging

Below is the full procedure for both conventional and CS-based PW imaging:

1. Transmit and acquire the raw data of  $K$  different PW insonifications, each corresponding to a unique angle  $\theta_k$ :
  - 1.1. Transmit the same pulse (whose parameters include central frequency, shape, apodization window, and number of cycles) from every channel with the appropriate delay in order to simulate a PW emitted with a steered angle of  $\theta_k$ ;
  - 1.2. Wait for and measure the raw data according to the desired range:  $[r_{min}, r_{max}]$ .
2. Obtain the beamformed image  $F_{\theta_k}$  for each angle  $\theta_k$ :
  - 2.1. Pre-process the raw data by applying a high-pass filter to remove any offset and a low-pass filter to remove electrical noise;
  - 2.2. Apply the desired reconstruction process to the pre-processed raw data according to the angle  $\theta_k$ , using either the conventional single PW imaging approach (Section 2.1.2) or the CS-based approach (Section 2.2.2) with a selected representation basis  $\Psi$ .
3. Coherently sum the  $K$  beamformed images  $F_{\theta_k}$  in order to obtain the compounded image  $\bar{F}$ .
4. Post-process  $\bar{F}$  using IQ demodulation to obtain  $I$ .
5. Normalize and log-compress  $I$  to obtain  $Bmode_{dB}$ , which is then visualized.

## 3 Demonstrator

As the UltrasoundToGo is funded by the Nano-Tera Initiative, the ongoing work has been presented every year at the Nano-Tera Annual Plenary Meeting. For this year's edition, it was the goal of the LTS5 lab to build a proof-of-concept of 2D CS-based PW imaging method. For this reason, a demonstrator was developed with the available hardware and software tools. The final product could also be used for educational purposes in order to familiarize oneself with US and CS.

Section 3.1 describes our complete physical and technological setup. Section 3.2 explains the available hardware and software provided by the *Ultrasound Advanced Open Platform* (ULA-OP) system [5]. Section 3.3 describes the software that we developed especially for conventional and CS-based PW imaging.

### 3.1 Complete Setup

Our physical setup can be seen in Figure 3.1. It consists of the following components:

1. ULA-OP system which can control up to 64 channels simultaneously;
2. Esaote PA230 128-element US probe (0.170 mm pitch and 2.25 MHz central frequency);
3. PC to control the ULA-OP device;
4. Two screens for visualization;
5. CIRS Model 054GS General Purpose US Phantom and US coupling gel;

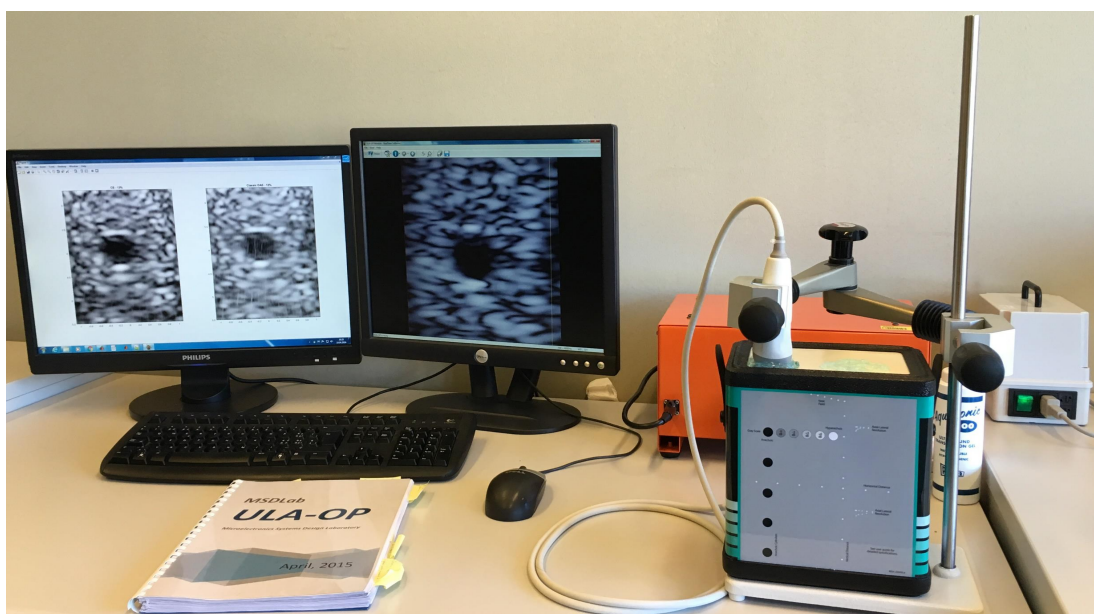


**Figure 3.1** Physical setup for the 2D CS-based PW imaging demonstrator.

6. Articulated arm and fixing clamps for maintaining the probe in a fixed position;
7. Support and stand for the CIRS phantom and the articulated arm.

In terms of software, the ULA-OP system includes two main user applications:

1. *ULA-OP Starter* for selecting a pre-defined imaging mode;
2. *ULA-OP Modula* for real-time visualization.

The ULA-OP hardware and software is explained with more detail in Section 3.2. For the demonstrator, we developed our own MATLAB software for US PW imaging (conventional and CS-based) that is compatible with the ULA-OP system. Through a Graphical User Interface (GUI), the following can be configured by a user:

1. Real-time visualization with the *ULA-OP Modula* application using the conventional B-mode imaging method. This is used for positioning the probe according to the user's preference (right-most computer screen in Figure 3.1).
2. Both CS-based and conventional PW imaging. This is computed off-line and the results are displayed afterwards (left-most computer screen in Figure 3.1).

A detailed description of the developed software for 2D US PW imaging can be found in Section 3.3.

## 3.2 Background on the ULA-OP System

The ULA-OP system was developed by the Microelectronics Systems Design Laboratory (MSDLab) at the University of Florence. According to the MSDLab, “ULA-OP was designed to allow the tests of new US methods including original beamforming strategies” [20]. This flexibility for incorporating original beamforming strategies is one of the reasons the ULA-OP system was selected. In this section, we will briefly describe the hardware and software already provided by the ULA-OP system. A detailed description can be found in the ULA-OP User Manual [20].

### 3.2.1 Hardware

The ULA-OP hardware consists of a metal container of dimensions  $33\text{ cm} \times 23\text{ cm} \times 18\text{ cm}$  that can be connected to a PC via USB 2.0. At the exterior of the container, there is a connector to attach a probe that can contain up to 192 elements. Inside the ULA-OP metal container, there are four Field-Programmable Gate Arrays (FPGA) that can each be assigned 16 channels of the probe, thus allowing the ULA-OP system to simultaneously control up to 64 ( $4 \times 16$ ) channels. These four FPGAs are devoted to applying conventional beamforming methods on the ULA-OP hardware itself.

### 3.2.2 Software

Two GUI applications are provided by the ULA-OP system in order to apply and visualize conventional US imaging techniques: the *ULA-OP Starter* and the *ULA-OP Modula*. The developers of ULA-OP have also created a MATLAB interface in order to define arbitrary US imaging methods and to launch a visualization from the MATLAB console.

#### *ULA-OP Starter* for Selecting a Mode

The ULA-OP device performs the transmission (TX) of US signals and reception (RX) of raw data through what is termed as a *mode*. A mode “identifies the probe, the TX-RX beamforming methods and TX sequences, the RX processing algorithm, and the display windows used in the real-time” [20].

The *ULA-OP Starter* application is used to operate the ULA-OP system under a pre-defined mode or one defined by a user.

### Configuring a Mode

The following files are needed to define a mode:

1. Probe configuration file (*\*.wks*), which specifies extensive information about a specific US probe, such as the *pitch*<sup>1</sup> and the number of transducers, in order to correctly perform focalization and beamforming in a real-time scenario. A very important specification also made with this file is the *pin mapping*, which maps the channels of the probe to the 64 memory blocks in the FPGAs.
2. Configuration file (*\*.cfg*), which identifies the name of the mode, links to the necessary *\*.ula* files for setting TX and RX parameters, sets the parameters for saving, and sets the parameters for the real-time visualization.
3. TX/RX strategy file (*\*.ula*), which specifies TX and RX parameters, such as number of elements, apodization, and focus.

In order to create an arbitrary imaging mode, which is required for our demonstrator since PW imaging is not already available on the ULA-OP system, the following files are also required:

1. BF TX file (*\*.bft*), which can be used to specify an arbitrary TX scheme and/or personalized waveforms.
2. BF RX file (*\*.bfr*), which can be used to specify an arbitrary RX scheme, such as defining delay and apodization waveforms.

A detailed description of each file and what parameters can be set is provided in the ULA-OP User Manual [20].

A software tool called *UlaOpConfigManager* makes it possible to read and edit the *\*.cfg* file. It can be launched from the *ULA-OP Starter* interface. From this tool, it is also possible to edit the *\*.ula* file(s) by opening the *TxRxStrategyEditor*. The BF TX and BF RX files can be created by using the *BF generator*, a MATLAB application with a GUI.

### ULA-OP Modula for Real-Time Visualization

When launching a mode through the *ULA-OP Starter* application, it is possible to provide a real-time visualization of the mode's results through the *ULA-OP Modula* application. As previously mentioned, the *\*.cfg* file is used to configure what is displayed. Through the GUI of the *ULA-OP Modula* application, it is possible to save the raw data and/or the beamformed data.

### Linking Between MATLAB and the ULA-OP System

With the *UOLink* MATLAB class it is possible to create a link between MATLAB and the ULA-OP system. It can be used within MATLAB to open the *ULA-OP Modula* application for real-time visualization and to save raw data and/or beamformed data.

## 3.3 Custom Software for the Demonstrator

Despite the multitude of software tools provided by the ULA-OP developers, they do not provide a convenient way of creating a mode for PW imaging. Moreover, the FPGAs in the ULA-OP system are

---

<sup>1</sup>The distance between the centers of transducers.

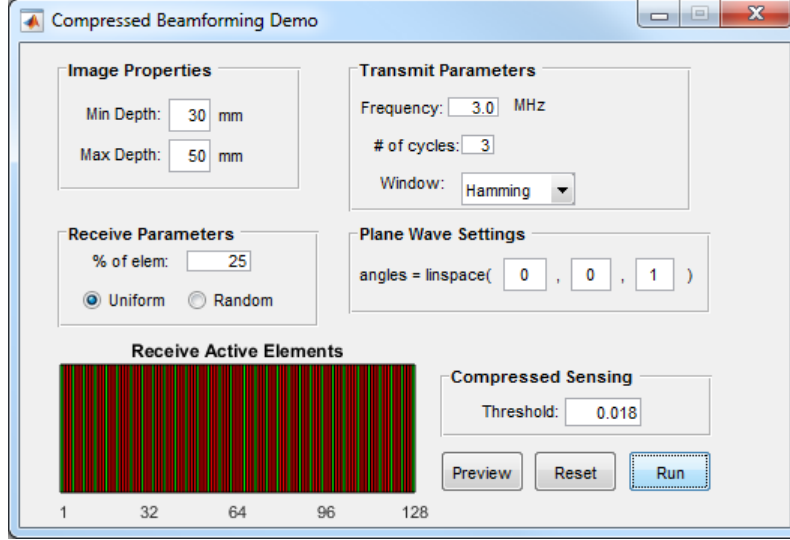


**Figure 3.2** GUI for the developed software for 2D CS-based PW imaging.

only able to perform conventional beamforming algorithms, such as DAS. Therefore, it was necessary to develop a software that could generate the required configuration files for a PW imaging mode (both conventional and CS-based) and then transfer the raw data to the computer for processing. We decided to develop our demonstrator in MATLAB as it is the only language that can interface with the ULA-OP system, by using the previously mentioned *UOLink* class. A MATLAB GUI was also developed so that a user could conveniently set a few of the parameters for PW imaging and CS.

Section 3.3.1 describes which parameters can be set by the GUI; Section 3.3.2 specifies additional parameters that can be set from a MATLAB main script; and Section 3.3.3 explains the main ULA-OP configuration issues that were resolved during our development process.

### 3.3.1 Graphical User Interface

A MATLAB GUI was developed in order to have a user-friendly demonstrator at the 2016 Nano-Tera Annual Plenary Meeting. The following parameters can be set from it:

1. Desired imaging range  $[r_{min}, r_{max}]$ ;
2. Percentage of elements to use (of a 128-element probe);
3. Uniform or random spacing of elements;
4. Transmission pulse (central frequency, number of cycles, apodization window);
5. Angles of multiple PWs (linearly spaced);
6.  $\beta_L$  parameter for the ADMM process (basis is hard-coded as *Orthogonal Wavelet*).

The demonstrator GUI is meant to be used as follows (refer to Figure 3.2):

1. Apply US coupling gel to the probe and to the surface on which the probe will be pressed against.
2. On the GUI, set the *Image Properties* for selecting a particular range and the *Transmit Parameters* for specifying the desired transmit pulse.
3. Press the *Preview* button to open the *ULA-OP Modula* application for a real-time visualization of the region being imaged by the probe. Adjust and lock the probe to the desired position with the articulated arm.
4. Set the *Receive Parameters*, the *Plane Wave Settings*, and the *Compressed Sensing* fields of the GUI. The window at the bottom left of the GUI shows which elements are active (in green) according



to the entries for *Receive Parameters*.

5. The conventional and CS-based PW imaging approaches can be performed off-line and compared by pressing the *Run* button. After completing both processes, a MATLAB figure is produced, showing the reconstruction for each method.

### 3.3.2 Full Capabilities in MATLAB

For the GUI, certain parameters were fixed as they did not need to be adjusted for the purpose of the Nano-Tera demonstrator. The main processing script that is called by the GUI when pressing *Run* has much more flexibility in setting the TX and RX settings. In particular, it can set the following (as well as those parameters that can be specified by the GUI):

1. Transmission pulse shape;
2. Arbitrary selection of elements for TX and RX;
3. Arbitrary angles for the multiple plane waves;
4. Additional CS parameters ( $\beta$  for signal integrity, the  $\Psi$  basis in which the beamformed signal is sparse, and number of iterations).

The full procedure of the main processing script is described below (the GUI follows the same procedure when pressing the *Run* button):

1. The user specifies their desired parameters at the top of the script (or in the GUI itself when using this tool).
2. The required configuration files are written: the *\*.cfg*, *\*.ula*, *\*.bft*, and *\*.bfr* files.
3. A link is created between MATLAB and the ULA-OP system with the *UOLink* interface.
4. The process described in Section 2.3 is performed for both conventional and CS-based PW imaging, using methods of the *UOLink* interface for acquisition and custom functions for the beamforming.
5. The results for both conventional and CS-based PW imaging are displayed side-by-side in a single MATLAB figure.

### 3.3.3 Main ULA-OP Configuration Issues and Solutions

The ULA-OP system did not allow complete flexibility due to some hardware constraints. The main issues are described here as well as our solution to these limitations.

#### Data handling

In order to apply our own beamforming method, the received raw data needs to be transferred to and saved on the disk of the PC that the ULA-OP is connected to. This is because the FPGAs in the ULA-OP system cannot be used to compute the CS-based beamforming for PW imaging. Unfortunately, the ULA-OP system does not provide a manner to transfer the raw data to the RAM of the computer. This introduces considerable latency as the data needs to be first transferred over USB 2.0 and then written to memory.

Nevertheless, the already available *UOLink* MATLAB interface allows the user to conveniently save various types of data at different points of the imaging scheme. We are interested in the *Pre-beamforming 12bit* data format (denoted with the extension *\*.rff12*). Through our main script, we are able to specify this data format and in the GUI implementation, this parameter is hard-coded. Another important file that gets saved to disk, alongside the *\*.rff12* file, is the *\*.uos* file. While the *\*.rff12* file contains all the received raw data for each emitted PW and for each active channel, the *\*.uos* file contains important

information that will allow us to correctly read and reorder the acquired data file. In particular, we are interested in the field **FirstBlock** within the **\*.uos** file.

When the ULA-OP system starts running, it cycles through the specified TX/RX schemes while continuously incrementing an index. Although the ULA-OP system wraps around to follow the same order of TX and RX schemes, the index being incremented starts at zero but does *not* wrap around. When the raw data begins to be stored, the index of the first recorded raw data is written into the field **FirstBlock** within the **\*.uos** file. From this value and the number of TX/RX schemes (in our case the number of steered PWs), we can deduce which angle corresponds to each set of raw data stored in the **\*.rff12** file. A simple reordering of the raw data is done in order to have the first set of raw data correspond to the first steered angle, the second set of raw data correspond to the second steered angle, etc.

### Selection of active elements

Only 64 elements of a probe can be simultaneously controlled by the ULA-OP system. However, in order to take advantage of all 128 elements of our probe, we use the **Sequencer** field of the **\*.cfg** file. The **Sequencer** field allows multiple TX/RX strategies (each defined by a unique **\*.ula** file) to be applied in a sequential order. Therefore, in order to access all elements of a probe, we can use a time-multiplexing approach by transmitting and receiving with all possible combinations of sets of 64 elements. In the case of our probe, we only need two sets if we want to use all 128 elements, and the **Sequencer** should cycle between four TX/RX strategies. Below is an example for the time-multiplexing approach with the **Sequencer** if we were to divide the channels into odd and even sets:

1. Transmit with odd set, receive with odd set;
2. Transmit with odd set, receive with even set;
3. Transmit with even set, receive with even set;
4. Transmit with even set, receive with odd set.

In reality, it is not actually possible to divide the 128 elements into odd and even sets with the current configuration. This is because certain combinations of elements are not possible due to the pin mapping of probe channels to the FPGA, which is defined in the **\*.wks** file. As previously mentioned, up to 64 channels of the probe can be controlled by the four FPGAs in the ULA-OP system. Each channel is pre-assigned to a memory block in the FPGA, with the possibility of multiple channels being assigned to a single memory block in the FPGA. Therefore, it is not possible to control channels that are assigned to the same memory block in the FPGA. As the even elements of the first 64 channels are assigned to the same memory blocks as the even elements in the last 64 channels (and the same is true for the odd elements), it is not possible to divide the 128 elements into odd and even sets.

For our demonstrator, we avoid this problem of active element selection by raising an error when the set of chosen active elements for a particular TX/RX scheme consists of any channels that are assigned to the same memory block in the FPGAs.

### Depth and range

For the **\*.rff12** format, the ULA-OP device can store up to 2688 samples per channel. As our sampling frequency is fixed to 50 MHz and the speed of sound in our medium is assumed to be  $1540 \text{ m s}^{-1}$ , 2688 samples corresponds to:

$$2688 \text{ samples} \times \frac{1 \text{ s}}{50 \times 10^6 \text{ samples}} \times \frac{1540 \text{ m}}{1 \text{ s}} = 82.8 \text{ mm}. \quad (3.1)$$

As sound needs to travel forward and backward, the ULA-OP can record a range of up to 41.4 mm.

Finally, we have noticed a strange phenomenon with respect to the allowed range for imaging: when the minimum depth is more than half of the maximum depth, the ULA-OP system tends to run into errors when recording the raw data. Therefore, in the case that the user defines a range that does not satisfy this condition, we set the minimum depth to the following to avoid an acquisition error:

$$r_{min} = r_{max}/2. \quad (3.2)$$

If this new minimum depth happens to be less than the one specified by the user, we acquire the data with the new minimum depth in order to safely measure the raw data. Then we crop the acquired data according to the user-specified minimum depth and process this cropped data.

## 4 Results and Analysis

In this section, several results obtained from the demonstrator are presented and discussed. Each subsection describes and analyzes a different test case. The same transmit pulse, with the following parameters, was used throughout the experimentation:

1. Transmit frequency of 3 MHz,
2. Number of cycles = 3.0,
3. Hamming apodization window.

Unless noted, only one PW ( $0^\circ$  incident angle) is emitted. The Esaote PA230 128-element US probe (0.170 mm pitch and 2.25 MHz central frequency) is used for TX and RX. We will be imaging the CIRS Model 054GS General Purpose US Phantom. The structures inside the phantom can be seen in Figure 4.1.

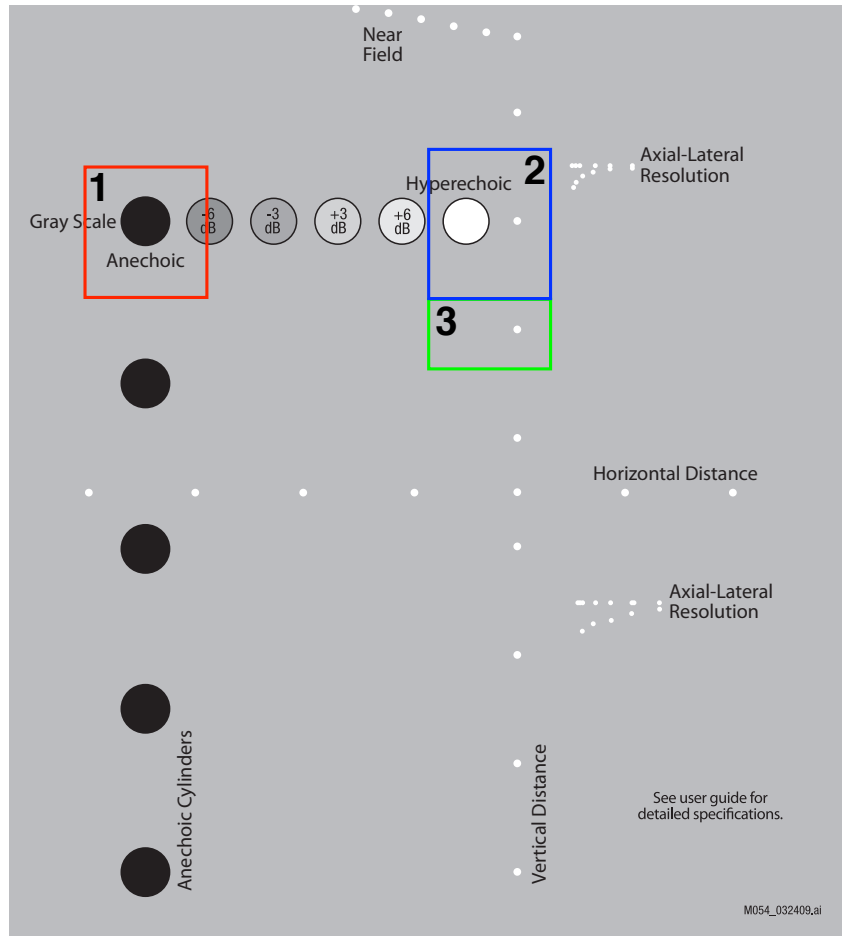


**Figure 4.1** CIRS Model 054GS General Purpose US Phantom [21].

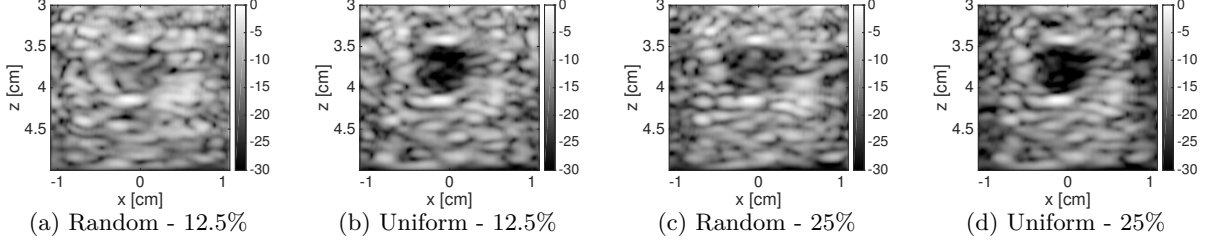


**Figure 4.2** B-mode images of the region surrounded in red and labeled “1” in Figure 4.1. Random spacing, (a) and (c), is compared with uniform spacing, (b) and (d), as a sensing scheme. Figures (a) and (b) use 12.5% of the elements while Figures (c) and (d) use 25% of the elements. A single PW with  $0^\circ$  incident angle is transmitted and the CS-based method with  $\beta_L = 0.018$  is used for image reconstruction.

## 4.1 Uniform vs. Random Sampling

As previously mentioned in Section 2.2.3, one key requirement for applying CS to US imaging is finding an appropriate sensing strategy. At the moment we will fix the representation basis to *Orthogonal Wavelets* and the  $\beta_L$  threshold to 0.018.

Two approaches were considered with regards to transducer arrangement: *uniform* spacing, where transducers are equidistant, and *random* spacing, where the outermost elements must be selected to span the entire probe but rest are chosen randomly following a uniform distribution.

As can be seen from Figure 4.2, a uniform spacing of elements clearly outperforms a random spacing of elements. The contrast for taking both 12.5% and 25% of the 128 elements is higher in the uniform case. Moreover, it is known that sidelobes are minimized when using uniform sampling [22]. For this reason, we use a uniform spacing of elements for the rest of the experiments.

## 4.2 Coherent Plane Wave Compounding

As mentioned in Section 2.1.2, a coherent summation of multiple PWs can increase the contrast of the final image. In this section, we provide results to validate this claim. As our probe already has low resolution, we decided to use just 5% of the probe elements so that the effect of compounding is more pronounced.

Figure 4.3 shows the impact of coherent PW compounding for the CS-based method. *Grating lobes* can be seen in the images for a single PW (Figure 4.3a) and three PWs (Figure 4.3b) as the strong reflector at  $x = 0$  cm and  $z = 4.1$  cm can roughly be observed on either side of it at around  $x = -0.6$  cm and  $x = 0.6$  cm. This is a common feature of under-sampled arrays, leading to these aliasing artifacts known as grating lobes. Coherent compounding can diminish these grating lobes for under-sampled arrays and in general reduce sidelobes, thus leading to an improvement in contrast. Steering a PW tilts the point

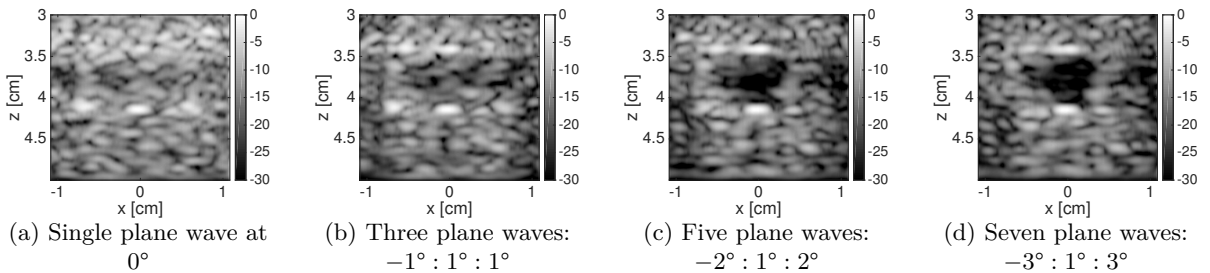


**Figure 4.3** B-mode images of the region surrounded in red and labeled “1” in Figure 4.1. A different number of PWs is transmitted for each image to show the effect of compounding. The CS-based approach with  $\beta_L = 0.018$  is applied for image reconstruction. Only 5% of the probe elements (uniformly spaced) are used.

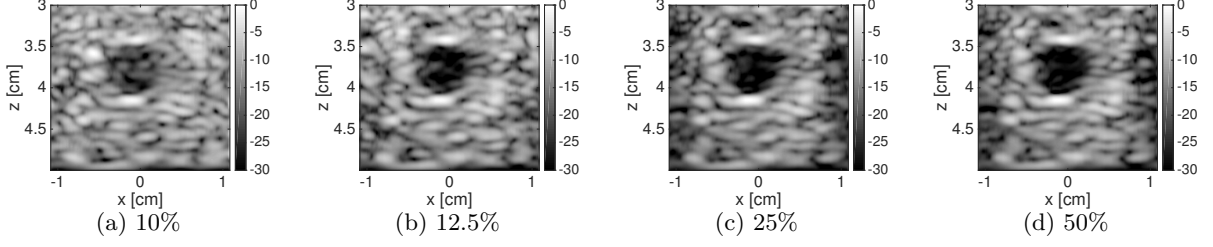


**Figure 4.4** B-mode images of the region surrounded in red and labeled “1” in Figure 4.1. The number of uniformly-spaced active elements is varied for each image: 10%, 12.5%, 25%, and 50% of the 128 elements. A single PW with  $0^\circ$  incident angle is transmitted and the CS-based PW beamforming method with  $\beta_L = 0.018$  is used for image reconstruction.

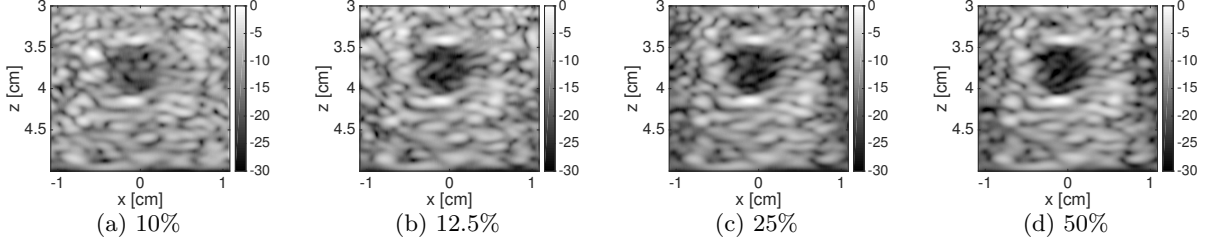


**Figure 4.5** B-mode images of the region surrounded in red and labeled “1” in Figure 4.1. The number of uniformly-spaced active elements is varied for each image: 10%, 12.5%, 25%, and 50% of the 128 elements. A single PW with  $0^\circ$  incident angle is transmitted and the conventional PW beamforming method is used for image reconstruction.

spread function (PSF) of a point source so that the PSFs interfere constructively at the true position of the point and destructively around the point to reduce grating lobes and sidelobes considerably.

### 4.3 Varying Number of Transducers

In this experiment, we observe how the number of active transducers affects the quality, in particular the contrast, of the resulting image. As can be seen from Figure 4.4 and Figure 4.5, the CS-based approach yields a higher contrast than the conventional PW imaging approach for each of the cases: 10%, 12.5%, 25%, and 50% of the 128 elements.

Furthermore, the contrast improves for both methods as the number of elements increases. When we increase the number of active channels, this yields more measured signals that can be used by the beamforming process. As beamforming is a coherent sum of signal values to estimate the intensity of a certain point, more signals should produce a better estimate of the intensity. A similar phenomenon was observed when increasing the number of PWs.

### 4.4 Choosing a Proper Representation Basis

At the moment, we have only been considering an anechoic object, and the *Orthogonal Wavelet* basis worked rather well in imaging such a structure. We will now consider hyperechoic elements and strong reflectors. For this experiment, we employ coherent PW compounding with five angles, linearly spaced from  $-2^\circ$  to  $2^\circ$ , and we use 12.5% of the probe elements.

As we can see from Figure 4.6a, the *Orthogonal Wavelet* (with a  $\beta_L$  threshold of 0.04) is able to capture the larger hyperechoic object on the left rather well but the contrast is not optimal for the smaller strong reflector on the right. This object on the right, however, can be better modeled as a point source using a *Dirac* basis for the CS-based approach.

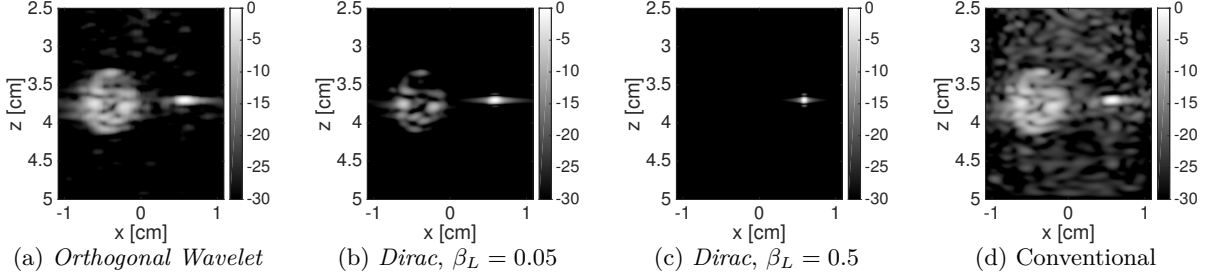


**Figure 4.6** B-mode images of the region surrounded in blue and labeled “2” in Figure 4.1. Five PWs, linearly spaced from  $-2^\circ$  to  $2^\circ$ , were transmitted using 12.5% elements of the probe, uniformly spaced. CS-based PW beamforming with compounding is used in (a)-(c) for image reconstruction: (a) uses the *Orthogonal Wavelet* basis with  $\beta_L = 0.04$ , (b) uses the *Dirac* basis with  $\beta_L = 0.05$ , and (c) uses the *Dirac* basis with  $\beta_L = 0.5$ . The last image (d) uses conventional PW beamforming with compounding.

Figures 4.6b-4.6c show the results for the same region when using the *Dirac* basis. Choosing a low value for  $\beta_L$  (Figure 4.6b), thus inducing less sparsity, is able to recover the larger hyperechoic object and the strong reflector. However, the larger object significantly loses its structure. We can observe, though, that the contrast of the strong reflector has improved, but there still remain significant sidelobes around it. These artifacts can be suppressed by increasing  $\beta_L$ , thus inducing more sparsity in the *Dirac* basis, as can be seen in Figure 4.6c. The contrast of the strong reflector has significantly improved and the sidelobes have diminished as compared to both Figures 4.6a and 4.6b but we have completely lost the larger hyperechoic object.

We can conclude that the structure of the object needs to be taken into account in order to select the appropriate representation basis. We have seen that the *Orthogonal Wavelet* basis is suitable for imaging anechoic and larger hyperechoic objects. Another important structure that the *Orthogonal Wavelet* basis can capture is *speckle*, which is granular texture that typically appears in a US image [1]. On the other hand, the *Dirac* basis is more suitable for imaging point sources such as the one seen in Figure 4.6, as it can significantly improve their contrast. However, the *Dirac* basis cannot capture textured objects such as larger hyperechoic objects and speckle.

This trade-off in selecting the appropriate representation basis motivates an approach which decomposes the image into strong reflector components and the rest, which can be denoted as *background* components. Such methods have already been investigated in the ultrasound community [23], [24]; however, not extensively in a CS setting.

## 4.5 Imaging Large Ranges

Finally, we analyze the performance of the CS-based approach when imaging larger ranges. As the current approach does not take into account the changing PSF shape at deeper depths, it will encounter difficulties for extended ranges.

At the moment, we have only considered ranges up to 2.5 cm so this issue has not arose. Unfortunately, the ULA-OP device does not allow us to image ranges larger than 4 cm due to storage constraints, but we will still be able to observe the limitations of the CS-based approach for this maximum allowable range.

As before, we apply coherent PW imaging with five angles, linearly spaced from  $-2^\circ$  to  $2^\circ$ , and we use 12.5% elements of the probe, uniformly spaced. The *Dirac* basis is chosen for the CS-based approach as the issue with imaging large ranges can be better observed with this choice of basis.

Figure 4.7 shows the results for imaging a similar region as in Figure 4.6 but extended by 1.5 cm for a total range of 4 cm. Figure 4.7a shows the result when setting  $\beta_L = 0.05$ . It can already be seen that

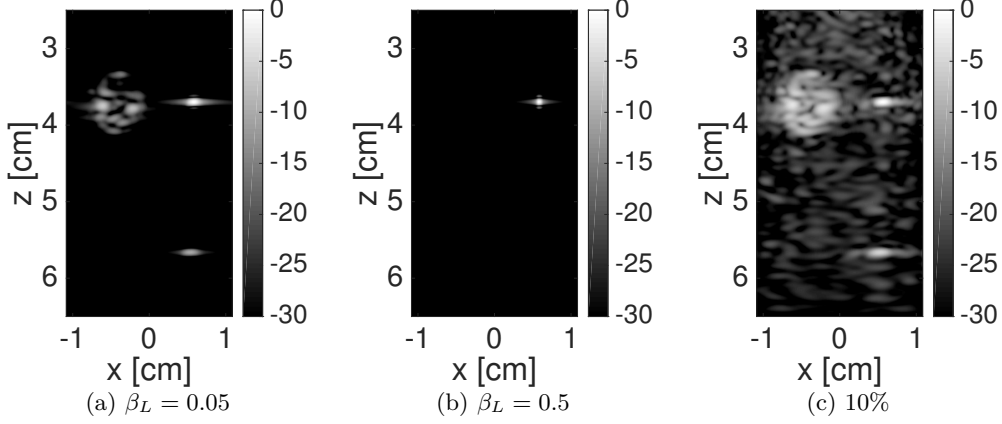


**Figure 4.7** B-mode images of the regions surrounded in blue and green and labeled “2” and “3” in Figure 4.1. Five PWs, linearly spaced from  $-2^\circ$  to  $2^\circ$ , were transmitted using 12.5% elements of the probe, uniformly spaced. CS-based PW beamforming with compounding is used in (a)-(b) for image reconstruction: (a) uses the *Dirac* basis with  $\beta_L = 0.05$  and (b) uses the *Dirac* basis with  $\beta_L = 0.5$ . The last image (c) uses conventional PW beamforming with compounding.

the point source at around 5.7 cm has a smaller intensity than the nearer one at around 3.7 cm. This is due to the fact that the PSF of the further strong reflector is more spread, *i.e.* the energy is less concentrated at the center. When we increase  $\beta_L$  to 0.5 in order to remove the sidelobes of the nearer strong reflector (Figure 4.7b), we notice that the strong reflector at around 5.7 cm is completely removed. Ideally, we would like to preserve both of the strong reflectors and remove the larger hyperechoic object on the left centered around 3.7 cm. However, this is not possible with the current CS-based PW imaging implementation as it assumes the same statistics for the entire image.

One solution to overcome this range limitation of the CS-based approach is to segment an image with a large range into smaller segments with shorter ranges and apply a different soft threshold  $\beta_L$  on each segment. The goal is to choose a segment length such that the standard deviation, *i.e.* width, of the PSF does not vary significantly within this limited range.



## 5 Conclusion

The project proved to be rather successful as we were able to build a user-friendly and smooth-running demonstrator for the Nano-Tera Annual Plenary Meeting. Although we faced several challenges by the ULA-OP system and are limited by certain hardware constraints, the final demonstrator serves its purpose as a proof-of-concept for CS-based PW imaging and the possible advantages over conventional PW imaging. Moreover, the demonstrator with its GUI can serve as a useful educational tool to familiarize oneself with US and CS in a very hands-on and practical setting.

The demonstrator also revealed certain features that could be added to improve the performance of the CS-based PW imaging method. The first is the introduction of a decomposition approach. It was observed that choosing the appropriate basis can make a significant impact in imaging certain types of structures, such as strong reflectors or more-textured elements, with high contrast. By building a model which is able to take into account different basis for the different type of structures, the quality of the final image could be improved. The second modification which could improve the performance of the CS-based approach is segmenting the image into horizontal strips, particularly when dealing with extended ranges. An approach that takes into account the increasing depth is needed since the PSF of reflectors gradually changes at deeper depths. Therefore, the same statistics cannot be assumed for the entire image. Both of these improvements for the CS-based PW imaging method are currently being investigated and developed. Furthermore, they are being tested with the hopes of submitting results by September 2016 for the IEEE IUS (International Ultrasonics Symposium) Plane-wave Imaging Challenge in Medical UltraSound (PICMUS) [25].

With regards to the demonstrator, there are also improvements that could be made. One such modification would be to add additional parameters that could be set from the GUI, such as the representation basis for CS. Finally, it would be wonderful to open source the software we have developed in PW imaging for the ULA-OP system in order to contribute to and receive feedback from the broader community of scientists and researchers in the field of medical US imaging. This move to an open platform would require porting the code to Python. Unfortunately, there is one huge drawback as the only way to interface with the ULA-OP device is through MATLAB. However, if we could obtain the source code, the shift towards an open source platform is certainly possible.

### Acknowledgments

I would like to thank Adrien Besson and Dimitri Perdios for their incredible patience and support during this project. They were wonderful supervisors that helped ease my introduction into the fields of ultrasound imaging and compressive sensing.

# Bibliography

- [1] T. Szabo, *Diagnostic Ultrasound Imaging: Inside Out*. Elsevier Academic Press, 2004.
- [2] F. Angiolini. (2016). UltrasoundToGo, [Online]. Available: <http://lsi.epfl.ch/page-93642-en.html>.
- [3] A. Ibrahim, P. Hager, A. Bartolini, F. Angiolini, M. Arditi, L. Benini, *et al.*, “Tackling the bottle-neck of delay tables in 3d ultrasound imaging”, in *Proceedings of the 2015 Design, Automation & Test in Europe Conference & Exhibition*, EDA Consortium, 2015, pp. 1683–1688.
- [4] G. D. Micheli. (2016). UltrasoundToGo, [Online]. Available: <http://www.nano-tera.ch/projects/359.php>.
- [5] P. Tortoli, L. Bassi, E. Boni, A. Dallai, Fr. Guidi, and S. Ricci, “ULA-OP: An advanced open platform for ultrasound research”, *Ultrasonics, Ferroelectrics, and Frequency Control, IEEE Transactions on*, vol. 56, pp. 2207–2216, 2009.
- [6] B. D. V. Veen and K. M. Buckley, “Beamforming: A versatile approach to spatial filtering”, *IEEE ASSP Magazine*, vol. 5, pp. 4–24, 1988.
- [7] M. Tanter and M. Fink, “Ultrafast imaging in biomedical ultrasound”, *Ultrasonics, Ferroelectrics, and Frequency Control, IEEE Transactions on*, vol. 61, pp. 102–119, 2014.
- [8] J. Bercoff, *Ultrafast Ultrasound Imaging*. INTECH Open Access Publisher, 2011.
- [9] G. Montaldo, M. Tanter, J. Bercoff, N. Benech, and M. Fink, “Coherent plane-wave compounding for very high frame rate ultrasonography and transient elastography”, *Ultrasonics, Ferroelectrics, and Frequency Control, IEEE Transactions on*, vol. 56, pp. 489–506, 2009.
- [10] J. Kirkhorn, “Introduction to IQ-demodulation of RF-data”, 1999.
- [11] M. Lustig, D. Donoho, and J. M. Pauly, “Sparse MRI: The application of compressed sensing for rapid MR imaging”, *Magnetic resonance in medicine*, vol. 58, pp. 1182–1195, 2007.
- [12] Chr. G. Graff and E. Y. Sidky, “Compressive sensing in medical imaging”, *Applied optics*, vol. 54, pp. C23–C44, 2015.
- [13] G. David, J.-l. Robert, B. Zhang, and A. F. Laine, “Time domain compressive beam forming of ultrasound signals”, *The Journal of the Acoustical Society of America*, vol. 137, pp. 2773–2784, 2015.
- [14] E. J. Candes and M. B. Wakin, “An introduction to compressive sampling”, *IEEE Signal Processing Magazine*, vol. 25, pp. 21–30, 2008.
- [15] R. G. Baraniuk, “Compressive sensing”, 2007.
- [16] Z. Han, H. Li, and W. Yin, *Compressive sensing for wireless networks*. Cambridge University Press, 2013.
- [17] S. Mallat, *A Wavelet Tour of Signal Processing, Third Edition: The Sparse Way*, 3rd. Academic Press, 2008.

# BIBLIOGRAPHY

- [18] J.-L. Starck, J. Fadili, and F. Murtagh, “The undecimated wavelet decomposition and its reconstruction”, *Image Processing, IEEE Transactions on*, vol. 16, pp. 297–309, 2007.
- [19] R. E. Carrillo, A. Besson, M. Zhang, D. Friboulet, Y. Wiaux, J. P. Thiran, *et al.*, “A sparse regularization approach for ultrafast ultrasound imaging”, in *Ultrasonics Symposium (IUS), 2015 IEEE International*, 2015, pp. 1–4.
- [20] *ULA-OP Manual*, Ver. 1.9, Microelectronics Systems Design Laboratory, 2015.
- [21] (2013). General purpose ultrasound phantom, [Online]. Available: <http://www.cirsinc.com/file/Products/054GS/054GS%20DS%20022415.pdf>.
- [22] B. D. Steinberg, “Principles of aperture and array system design: Including random and adaptive arrays”, *New York, Wiley-Interscience, 1976. 374 p.*, vol. 1, 1976.
- [23] Y. Yankelevsky, Z. Friedman, and A. Feuer, “Component Based Modeling of Ultrasound Signals”, pp. 1–14, 2016.
- [24] T. Szasz, A. Basarab, and D. Kouamé, “Strong reflector-based beamforming in ultrasound medical imaging”, *Ultrasonics*, vol. 66, pp. 111–124, 2016.
- [25] (2016). Plane-wave Imaging Challenge in Medical UltraSound, [Online]. Available: [https://www.creatis.insa-lyon.fr/Challenge/IEEE\\_IUS\\_2016/](https://www.creatis.insa-lyon.fr/Challenge/IEEE_IUS_2016/).